ARTICLES

Journal of Semiconductors
(2023) 44, 052701
doi: 10.1088/1674-4926/44/5/052701

One-photo excitation pathway in 2D in-plane heterostructures for effective visible-light-driven photocatalytic degradation

Mengchi Liu, Yiwen Cheng, Yuee Xie, Yingcong Wei, Jinhui Xing, Yuanping Chen†, and Jing Xu†

School of Physics and Electronic Engineering, Jiangsu University, Zhenjiang 212013, China

Abstract: Broad-spectrum absorption and highly effective charge-carrier separation are two essential requirements to improve the photocatalytic performance of semiconductor-based photocatalysts. In this work, a fascinating one-photon system is reported by rationally fabricating 2D in-plane Bi_2O_3/BiOCl (i-Cl) heterostructures for efficient photocatalytic degradation of RhB and TC. Systematic investigations revealed that the matched band structure generated an internal electric field and a chemical bond connection between the Bi_2O_3 and BiOCl in the Bi_2O_3/BiOCl composite that could effectively improve the utilization ratio of visible light and the separation effectivity of photo-generated carriers in space. The formed interactions at the 2D in-plane heterojunction interface induced the one-photon excitation pathway which has been confirmed by the experiment and DFT calculations. As a result, the i-Cl samples showed significantly enhanced photocatalytic efficiency towards the degradation of RhB and TC (RhB: 0.106 min^{-1}; TC: 0.048 min^{-1}) under visible light. The degradation activities of RhB and TC for i-Cl were 265.08 and 4.08 times that of pure BiOCl, as well as 9.27 and 2.14 times that of mechanistically mixed Bi_2O_3/BiOCl samples, respectively. This work provides a logical strategy to construct other 2D in-plane heterojunctions with a one-photon excitation pathway with enhanced performance.

Key words: photocatalysis; CAU-17; Bismuth oxyhalides; one-photon excitation pathway; 2D in-plane heterojunction

Citation: M C Liu, Y W Cheng, Y E Xie, Y C Wei, J H Xing, Y P Chen, and J Xu, One-photo excitation pathway in 2D in-plane heterostructures for effective visible-light-driven photocatalytic degradation[J]. *J. Semicond.*, 2023, 44(5), 052701. https://doi.org/10.1088/1674-4926/44/5/052701

1. Introduction

In the past few decades, environmental pollution has become increasingly serious and was caused by organic pollutants, especially organic dyes produced in chemical production and antibiotics widely used in medical treatment[1–3]. Wastewater containing organic dyes is carcinogenic and mutagenic to the human body after contact[4, 5]. Antibiotics will not only cause chemical pollution but also enhance the drug resistance of bacteria after entering the water quality, thus posing a threat to human public health[6]. So far, various technologies have been developed to solve the problem of wastewater pollution, such as adsorption, electrochemistry, photocatalysis, ozone oxidation, and precipitation[7–11]. It is optimal to use green and efficient photocatalysis technology to treat wastewater.

In recent years, BiOCl is considered a promising photocatalyst because of its chemical stability and typical layered crystal structure[12–15]. However, the low visible light utilization rate and wide band gap greatly limit the application in the visible light photocatalysis field. The construction of the heterojunction is a potential method to overcome these shortcomings[16–21]. The heterojunction is usually constructed by coupling two semiconductors together to promote the separation and transmission of charge and adjust the energy band gap of the material to improve the utilization rate of visible light. At present, there have been some reports about the heterojunctions of BiOCl with enhanced photocatalytic performance, such as BiOCl/Mn_3O_4[22], BiOCl/CuO[23] and BiOCl/$BiPO_4$[24]. These heterostructures design two-photon excitation paths to improve the separation and transmission efficiency of photo-generated carriers, such as type-II or Z scheme heterostructures[8,25–27]. However, in principle, the photon utilization rate of the two-photon excitation pathway will decrease by 50% under the irradiation of a monochromatic light source. Thus, the one-photon excitation pathway (Fig. 1(a)) is more favorable, which can be obtained by forming a heterojunction between a semiconductor with a suitable bandgap and a semiconductor with a large bandgap[28, 29]. Moreover, most traditional heterojunctions have poor photo-excited charge separation/transport characteristics than 2D in-plane heterojunctions (Figs. 1(b) and 1(c))[30, 31]. Based on the above analysis, the construction of a 2D in-plane heterojunction with a one-photon excitation pathway is a promising method to improve photocatalytic efficiency under visible light. Metal-organic frameworks (MOFs) and their derivatives have become a research hotspot because of their porous crystalline structure and abundant surface properties[32]. In 2016, CAU-17 was first synthesized and considered as the preparation cost which is the lowest among Bi-MOFs[33, 34]. Zhu *et al.* obtained a BiOBr/CAU-17-2h photocatalyst with CAU-17 as the precursor, which showed excellent performance in removing 90% rhodamine b within 50 min[35]. Yang *et al.* designed the Bi_2WO_6/CAU-17 composite photocatalyst, and the best sample showed the photocatalytic degradation performance of 90% methyl blue in 60 min[36]. Therefore, BiOCl nanosheets can grow in situ on CAU-17 micron-rod via a halogenation process to avoid the aggregation of individu-

Correspondence to: Y P Chen, chenyp@ujs.edu.cn; J Xu, xjing@ujs.edu.cn
Received 13 JANUARY 2023; Revised 7 FEBRUARY 2023.

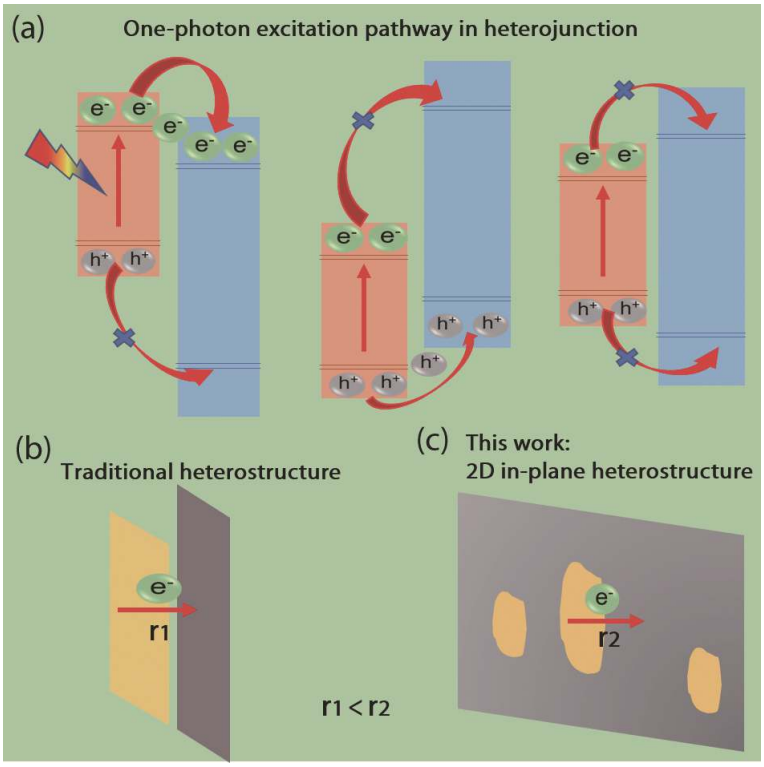

Fig. 1. (Color online) The photo-generated carrier transport diagram (a) via one-photon excitation pathway and (b, c) in traditional heterostructure and 2D in-plane heterostructure.

al BiOCl nanosheets.

Herein, in-plane Bi_2O_3/BiOCl (i-Cl) heterostructures were synthesized for boosted photocatalytic degradation of RhB and TC by a one-photon excitation pathway of visible light. The novel in-plane heterostructure structure endows the BiOCl-based photocatalyst with efficient spatial carrier separation and intense light absorption capability. As a result, the optimized i-Cl composite shows enhanced photocatalytic efficiency compared to those of pure BiOCl and Bi_2O_3, as well as mechanistically mixed Bi_2O_3/BiOCl samples. The RhB and TC degradation activities of the optimum i-Cl sample show a remarkable 265.08-fold and 4.08-fold enhancement compared with pristine BiOCl. This work provides a logical strategy to construct other 2D in-plane heterojunctions with a one-photon excitation pathway with enhanced performance.

2. Experimental section

2.1. Chemicals

1,3,5-benzene tricarboxylic acid (H_3BTC), bismuth nitrate pentahydrate ($Bi(NO_3)_3{\cdot}5H_2O$), N, N-dimethylformamide (DMF), methanol anhydrous (MeOH), ethanol, ammonium bromide (NH_4Br), ammonium iodide (NH_4I), and ammonium chloride (NH_4Cl), were all untreated pure samples. The experimental water is deionized.

2.2. Synthesis of CAU-17

According to the previous report[37], CAU-17 was synthesized by the solvothermal method. Firstly, 55 mL MeOH and 5 mL DMF were added into a 100 mL beaker with 1 mmol $Bi(NO_3)_3{\cdot}5H_2O$. Then, 3 mmol H_3BTC was dissolved into the reaction mixture and stirred at room temperature for 30 min. The mixed solution was sealed into a 100 mL polytetrafluoroethylene-lined autoclave for 24 h with the oven temperature set at 120 °C. The resulting samples were washed with MeOH and DMF and dried in an oven for 12 h at a temperature of 60 °C.

2.3. Synthesis of i-X (X = Cl, Br, I)

In-plane Bi_2O_3/BiOX (X = Cl, Br, I) photocatalysts were obtained via the water bath method. Firstly, 50 mL of deionized water was added into a 100 mL triangular bottle with 10 mmol of NH_4X (X = Cl, Br, I). Under stirring, 0.5 g of CAU-17 was added into the above triangular bottle and placed in a water bath pot for 1h, and the temperature was set at 90 °C. The obtained sample was washed several times with pure water and dried. After that, the resulting powder was placed in a muffle furnace and kept at 450 °C for 2 h, and the heating rate was 2 °C /min. The products were named i-X (X = Cl, Br, I), respectively. In addition, the Bi_2O_3 sample was obtained by directly calcining CAU-17.

2.4. Synthesis of t-Cl

For comparison, BiOCl was synthesized by primitive hydrothermal method. Then, the traditional Bi_2O_3/BiOCl sample was obtained by a simple electrostatic-driven self-assembling method, which was named t-Cl. A certain amount BiOCl and Bi_2O_3 were added into 60 mL of ethanol and stirred at 60 °C until the solvent evaporated. The molar ratio of BiOCl and Bi_2O_3 was 5 : 1, which was consistent with the proportion in the i-Cl sample.

2.5. Photocatalytic degradation reaction

The photocatalytic performance of the prepared samples was evaluated by photocatalytic degradation of RhB (10 mg/L), TC (10 mg/L), and the mixed solution of RhB (10 mg/L) and TC (10 mg/L) under visible-light irradiation. In the degradation system, a 300 W Xe lamp with a 420 nm cut-off filter was used as the light source. Meanwhile, 10 mg of the photocata-

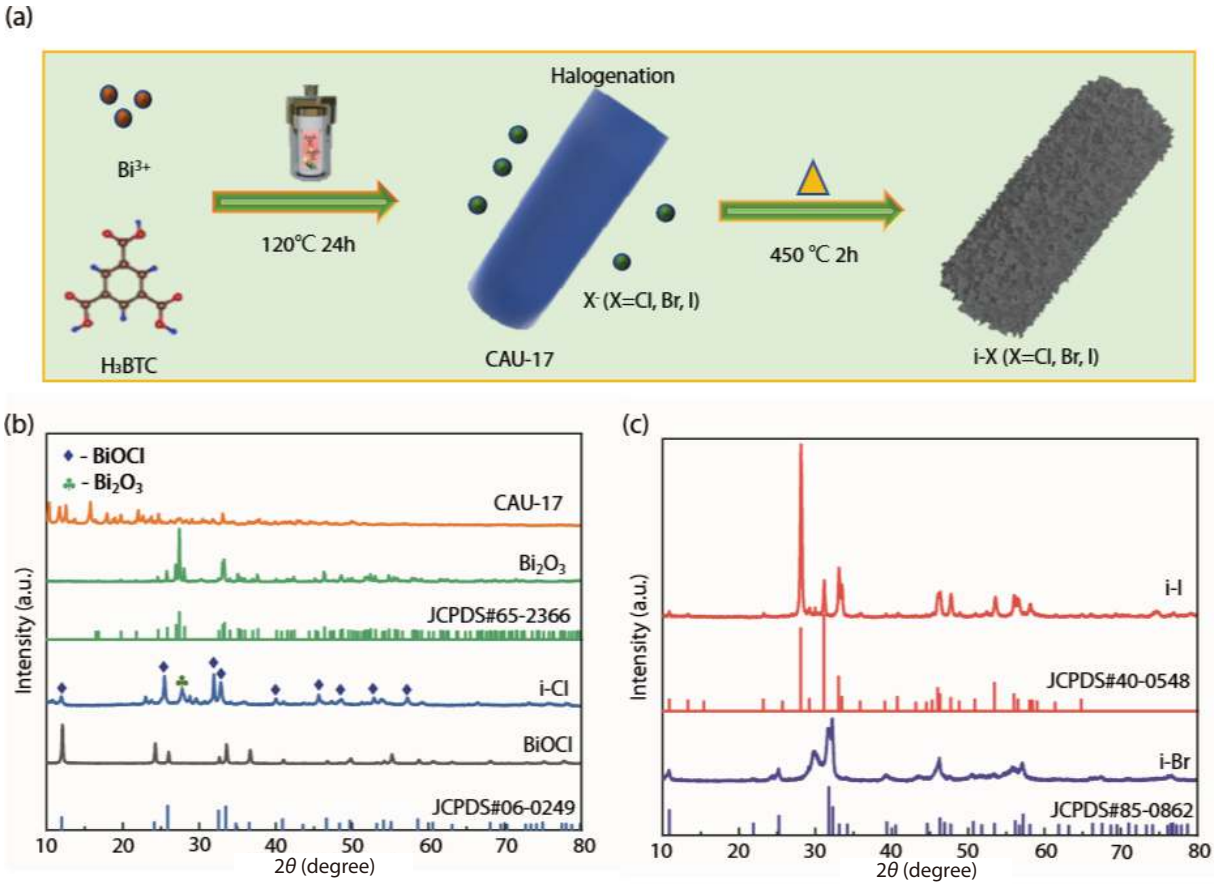

Fig. 2. (Color online) (a) Schematic illustration for the synthesis of i-X (X = Cl, Br, I). (b, c) XRD patterns of CAU-17, $B_{i2}O_3$, i-Cl, BiOCl, i-I, and i-Br.

lyst was added into 50 mL RhB (10 mg/L), TC (10 mg/L) aqueous solution, and a mixed aqueous solution of RhB (10 mg/L) and TC (10 mg/L), respectively. Then, the mixture should be stirred in the dark for 30 min to reach the adsorption-desorption equilibrium. Then, the beaker was irradiated under visible light and 3 mL of water was extracted every 5 min. After that, dye and antibiotic solution concentration was determined on a UV-vis spectrophotometer at the wavelengths of 554 and 357 nm for RhB and TC, respectively.

In addition, the synthesis of BiOCl, DFT calculation, and characterizations were introduced in the supporting information.

3. Results and discussion

3.1. Materials characterizations

As shown in Fig. 2(a), samples including CAU-17, Bi_2O_3/BiOCl (i-Cl), Bi_2O_3/BiOBr (i-Br) and Bi_2O_3/BiOI (i-I) were prepared. The XRD analysis was performed to analyze the structure of CAU-17, Bi_2O_3, i-Cl, BiOCl, i-I, and i-Br samples. The XRD pattern of CAU-17 was almost consistent with the previously reported literature[37], demonstrating the successful synthesis of CAU-17. As shown in Fig. 2(b), the pattern of Bi_2O_3 without halogenation treatment is consistent with that of Bi_2O_3 (JCPDS#65-2366), which indicates that bismuth-base CAU-17 was converted into Bi_2O_3 during the calcination process. The major characteristic peaks located at 11.92°, 25.38°, 31.86°, 32.84°, 39.94°, 45.68°, 48.38°, 52.78°, 57.19° marked with the diamond symbol of i-Cl are ascribed to BiOCl (JCPDS#06-0249)[38] and the peak located at 27.71° marked with plum blossom symbol vest in Bi_2O_3[39]. Moreover, it can be seen from Fig. 2(c) that the major peaks of i-I and i-Br are highly corresponding to Bi_5O_7I (JCPDS#40-0548) and BiOBr (JCPDS#85-0862), respectively[40, 41].

The morphologies of i-X (X = Cl, Br, I) samples were observed by a scanning electron microscope (SEM). As shown in Fig. S1, the morphology of CAU-17 displayed rod-like morphologies, which was consistent with the previous paper[34]. The rod-shaped frame was retained and the nanosheets with a thickness of 20 nm were accumulated on the rod-shaped surface in layers. Moreover, the transmission electron microscope (TEM) and high-resolution transmission electron microscope (HR-TEM) images were obtained to further analyze the lattice structure of the i-Cl sample. The lattice spacings of 0.275 and 0.32 nm corresponding to the (110) lattice plane of BiOCl and (201) crystal plane of Bi_2O_3[42], respectively, appeared in the central area of the nanosheet (Fig. 3(c)), confirming the formation of in-plane Bi_2O_3/BiOCl heterostructures. The EDS mapping was carried out and the images were presented in Figs. 3(d)–3(f). The images indicated the existence of Bi (blue), O (green), and Cl (red) elements, and all the elements were distributed on the CAU-17 rod frame. The atomic fraction and mass fraction of the three elements were recorded in Table S1. The molar ratio of BiOCl to Bi_2O_3 in the i-Cl sample can be calculated to be about 5 : 1. The energy dispersive X-ray (EDX) line profile of the i-Cl sample (Fig. 3(g)) shows that the spatial distribution of the three elements is obvious inhomogeneous. There were obvious differences after the fabrication of core-shell structure, which further confirms that the i-Cl sample is heterogeneous. Fig. S2 shows the SEM images of the i-I and i-Br samples. Their morphologies all retained the rod-shaped frame of CAU-17 and the nanosheets ac-

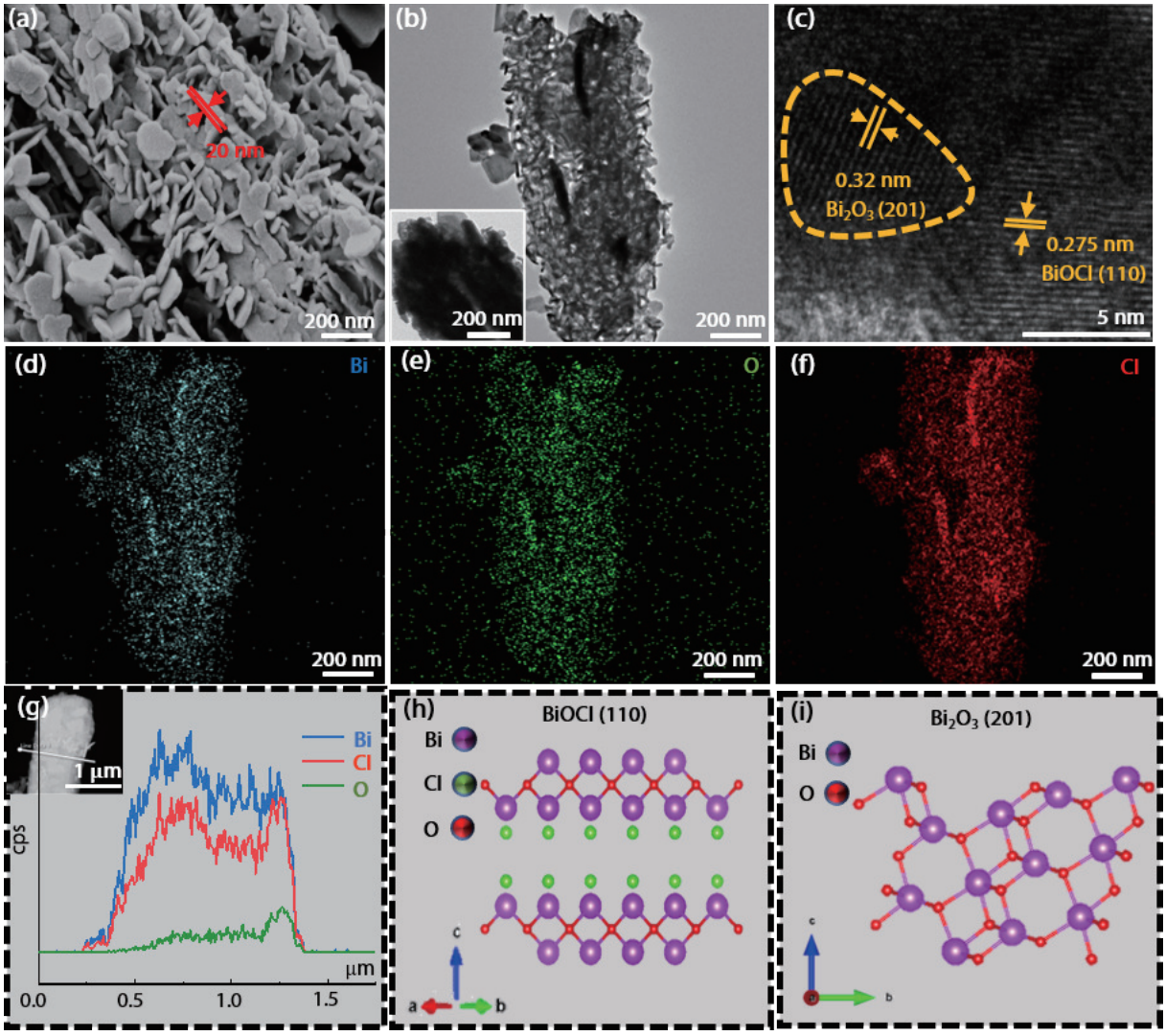

Fig. 3. (Color online) (a) SEM images, (b) TEM, (c) HR-TEM images, (d–f) EDS mapping images and (g) EDX line profile result of i-Cl sample; Atomic structures of (h) BiOCl (110) and (i) Bi_2O_3 (201).

cumulated on the rod-shaped surface. Atomic structures of BiOCl (110) and Bi_2O_3 (201) were shown in Figs. 3(h) and 3(i).

X-ray photoelectron spectroscopy (XPS) was conducted to elucidate the element composition and chemical state of the samples. Fig. 4(a) shows the survey spectra of BiOCl, Bi_2O_3, and i-Cl samples. As shown in Fig. 4(b), for pure BiOCl, the two peaks of Bi $4f_{5/2}$ and Bi $4f_{7/2}$ at 165.21 and 159.90 eV demonstrate Bi is +3 oxidation state[43]. Compared with BiOCl, the Bi 4f peaks of i-Cl show similar two symmetrical peaks and shift to the smaller binding energy. The Bi 4f spectra of Bi_2O_3 show the peaks at 164.17 and 158.89 eV indicating that Bi exists in a +3 oxidation state[44]. As shown in Fig. 4(c), the migration trend of O 1s is similar to that of Bi 4f. The spectra of Cl 2p are shown in Fig. 4(d). It can be seen that the peaks at 200.19 and 198.59 eV for BiOCl are assigned to Cl $2p_{1/2}$ and Cl $2p_{3/2}$. For i-Cl, the Cl 2p peaks shift to the smaller binding energy indicating that the built-in electric field will be generated between BiOCl and Bi_2O_3, and the charge will be transferred from Bi_2O_3 to BiOCl[45].

3.2. Evaluations of photocatalytic performances

The photocatalytic performances of the prepared samples were investigated by RhB, TC, and mixed wastewater with TC and RhB degradation under visible light. The photocatalytic degradation comparison results of i-X (X = Cl, Br, I) samples are shown in Figs. S4 and S5. Among the three samples, i-Cl has the best degradation rate constant. The RhB degradation rate constant of i-Cl is 4.25-fold that of i-Br and 2.72-fold that of i-I, respectively. The TC degradation rate constant of i-Cl is 2.41-fold that of i-Br and 2.17-fold that of i-I, respectively. Photocatalytic degradation comparison results of i-Cl, Bi_2O_3, BiOCl, and traditional Bi_2O_3/BiOCl (t-Cl) are shown in Figs. 5 and 6. As shown in Fig. 5(a), the concentration of RhB decreased with increasing reaction time overall photocatalysts. The RhB degradation rate of the four samples from low to high is BiOCl, Bi_2O_3, t-Cl, and i-Cl, and the degradation rate reached 3%, 7%, 22%, and 90% in 20 min, respectively. It can be seen that BiOCl and Bi_2O_3 samples can hardly degrade RhB, the RhB degradation rate of the t-Cl sample was increased by 15% and the degradation efficiency of the i-Cl sample was greatly improved compared with t-Cl samples due to its good interface effect. Fig. 5(b) shows the degradation rate of RhB follows quasi-first-order kinetics. The kinetic constant (k) of i-Cl is 9.3-fold that of t-Cl. Fig. 5(c) shows the TC degradation rate of the four samples. The TC degradation rate of the four samples from high to low is i-Cl, t-Cl, Bi_2O_3, and BiOCl, and the degradation rate reached 25%, 30%, 40%, and 70% in 20 min, respectively. In addition, Fig. 5(d) shows

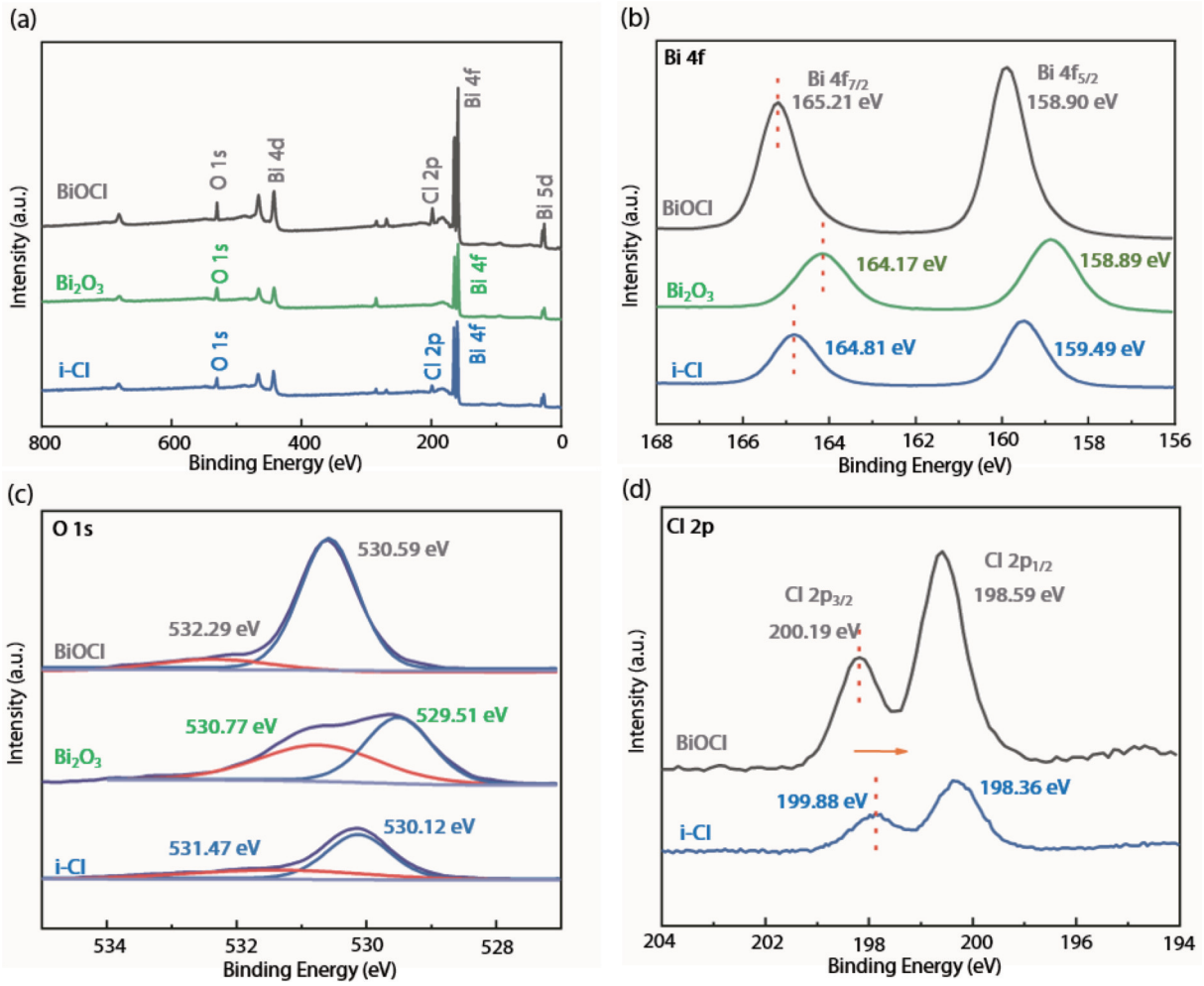

Fig. 4. (Color online) XPS spectra of BiOCl, i-Cl, and Bi_2O_3 samples: (a) survey spectra, (b) Bi 4f, (c) O 1s, (d) Cl 2p.

that the TC degradation rate of all photocatalytic systems follows quasi-first-order kinetics. The *k* value of i-Cl is 2.14-fold that of t-Cl. The photocatalytic performance of i-Cl was compared with some BiOCl-based catalysts previously reported in Tables S2 and S3. It is found that i-Cl has a higher degradation rate constant than these catalysts. Therefore, the remarkable activity of i-Cl makes it a valuable photocatalyst for removing organic pollutants.

The photocatalytic mixed wastewater with RhB and TC degradation rates of various samples are shown in Fig. 6. As shown in Figs. 6(a) and 6(c), the photocatalytic RhB and TC degradation rates of i-Cl samples are 64% and 65% in 20 min. Compared with the degradation of RhB and TC alone, the degradation rate of RhB decreased by 26% and the degradation rate of TC decreased by 5%. It can be seen that the i-Cl sample can degrade RhB and TC simultaneously under visible-light irradiation. Compared with the i-Cl sample, the TC degradation rate of the t-Cl samples was almost unchanged, and the degradation rate of RhB was reduced by 20%. BiOCl and Bi_2O_3 samples still cannot degrade RhB, but the degradation rate of TC was basically unchanged. Figs. 6(b) and 6(d) showed the corresponding *k* values of RhB and TC degradation in the mixed wastewater photocatalytic systems. In summary, the TC degradation rates of the four samples are all almost unchanged. BiOCl and Bi_2O_3 cannot degrade RhB and the RhB degradation rate of BiOCl and t-Cl samples decrease by over 20%, which may be that TC has more advantages in the competitive adsorption on the surface of photocatalyst[46]. Fig. S6 shows the UV-vis curves of different aqueous solutions over i-X (X = Cl, Br, I) samples. In addition, the cycling ability of the i-Cl sample on mixed wastewater with TC and RhB degradation was evaluated. As shown in Fig. S7(a), the degradation activity decreased only slightly after four cycles. Fig. S7(b) shows the comparison of XRD patterns of the i-Cl sample before and after the recycling process. It can be seen that the peak position has shifted, but the major peaks only changed a little. These results indicate i-Cl sample has good stability in the photocatalytic degradation of mixed wastewater with TC and RhB.

3.3. Optical and electrical properties

The results of UV-vis DRS were exhibited in Fig. 7(a). It can be seen that the obvious absorption edges of BiOCl and Bi_2O_3 are located at 368 and 443 nm, respectively. Compared with the pristine BiOCl sample, the i-Cl and t-Cl samples exhibit an obvious red shift and enhanced UV and visible-light harvesting, which is due to the existence of Bi_2O_3 with strong light-harvesting capability. This extended light absorption is beneficial to the photocatalytic reaction.

The photoluminescence (PL) spectra were tested in Fig. 7(b). It can be seen from Fig. 7(b) that the pristine BiOCl displays a prominent emission peak, suggesting the intense recombination of carriers inside BiOCl. After combining with Bi_2O_3, the PL intensity of i-Cl and t-Cl heterojunctions decrease slightly compared to pristine BiOCl, implying that the

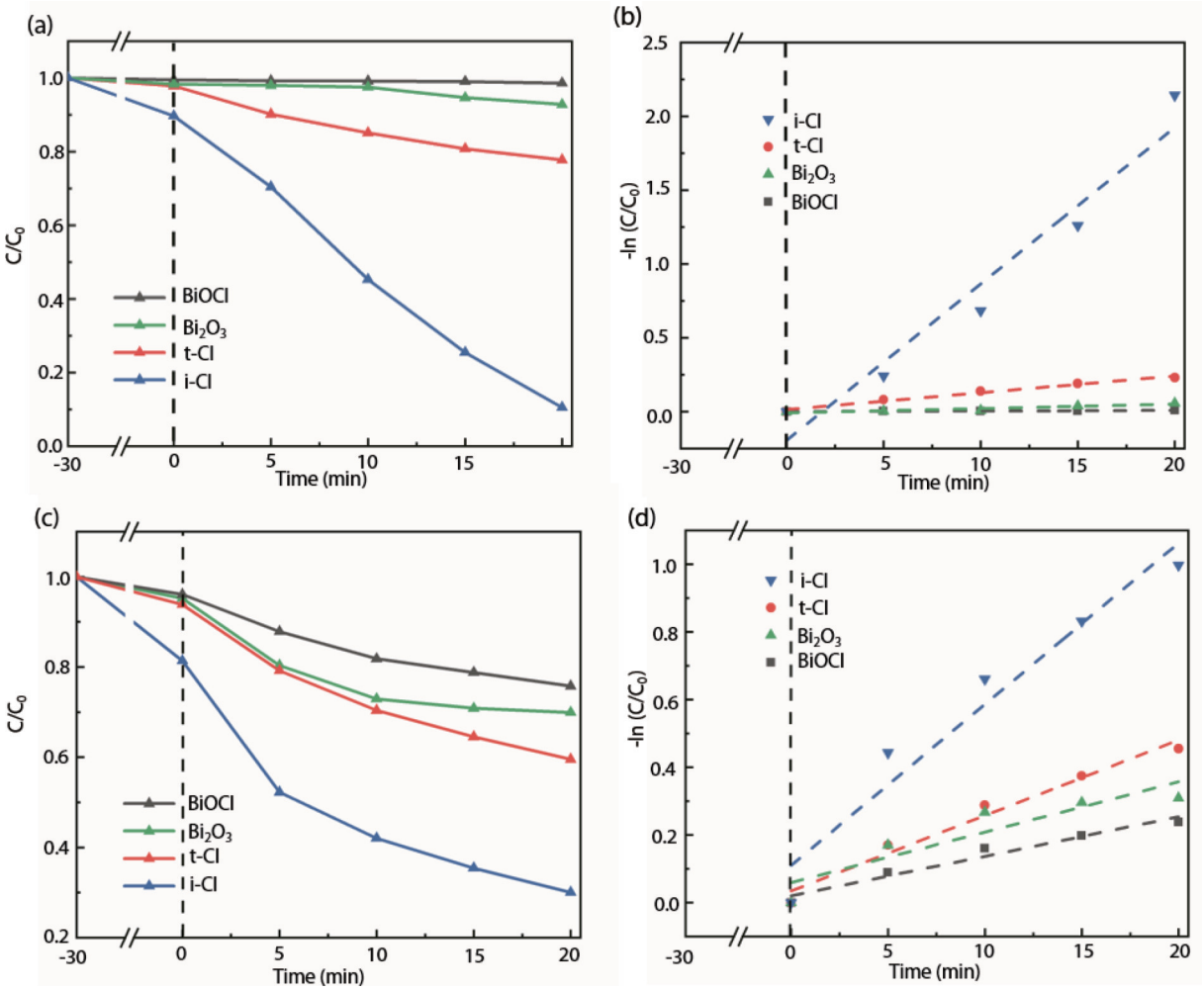

Fig. 5. (Color online) (a) The photocatalytic RhB degradation curves and (b) first-order kinetic fitting of curves of i-Cl, t-Cl, Bi_2O_3, and BiOCl samples. (c) The photocatalytic TC degradation curves and (d) first-order kinetic fitting of curves of i-Cl, t-Cl, Bi_2O_3, and BiOCl samples.

presence of Bi_2O_3 could retard the electron-hole recombination. t is worth noting that the PL intensity of the i-Cl heterojunction is lower than that of the t-Cl heterostructure, revealing the superiority of monodispersed and in-plane heterostructure for suppressing the recombination of photocarriers[47]. Surface photovoltage (SPV) spectra of BiOCl, Bi_2O_3, and i-Cl samples were shown in Fig. 7(c). It can be seen that i-Cl showed a stronger photovoltage in the visible range compared with BiOCl, which indicated that i-Cl can respond under visible light irradiation. And i-Cl showed higher photovoltage than Bi_2O_3 due to lower electron-hole recombination[48]. Photocurrent responses and electrochemical impedance spectra (EIS) test are recorded in Figs. 7(d) and 7(e). Among all the samples, the i-Cl sample exhibited the highest photocurrent response and smallest semicircle, revealing the most accelerated photocarrier separation efficiency.

3.4. Photocatalytic mechanism

According to the absorption spectra of BiOCl and Bi_2O_3, the corresponding band gaps of a semiconductor were calculated by the Tacu Plot formula[49]:

$$(ahv)^{1/2} = A(hv - E_g). \quad (1)$$

Therefore, the band gap of Bi_2O_3 and BiOCl can be calculated as 2.80 and 3.37 eV (Fig. 8(a)). Fig. 8(b) shows the valence band (VB) values of Bi_2O_3 and BiOCl. Then, the conduction band (CB) values are 0.35 and –0.29 V of Bi_2O_3 and BiOCl according to the coming formula:

$$E_{CB} = E_{VB} - E_g. \quad (2)$$

The band structures of Bi_2O_3 and BiOCl samples before and after contact are shown in Fig. 8(c). When BiOCl contacts Bi_2O_3, the built-in electric field will be generated at the interface between BiOCl and Bi_2O_3. To know the direction of the carrier transfer of the internal electric field (IEF) between the Bi_2O_3/BiOCl heterojunction, the charge density difference of the BiOCl/Bi_2O_3 heterojunction and work functions of Bi_2O_3 (201) and BiOCl (110) were calculated by DFT simulation. It can be seen from Fig. 8(d) that charge transfer from BiOCl to Bi_2O_3. It can be seen from Figs. 8(e)–8(f) that the fermi level of Bi_2O_3 (201) is higher than that of BiOCl (110), which further demonstrated that charge transfer from BiOCl to Bi_2O_3 when they are closely contacted by IEF between BiOCl and Bi_2O_3.

The reactive species trapping experiment of the i-Cl sample was carried out to analyze the major active substances during the mixed wastewater degradation system. Benzoquinone (BQ), disodium EDTA (EDTA-2Na), and isopropyl alcohol (IPA) are used as scavengers for superoxide radical ($\cdot O_2^-$)[50], photoinduced holes (h^+)[51] and hydroxyl radical ($\cdot OH$)[52], respectively. As shown in Fig. 9(a), IPA and EDTA-2Na had a great effect on the degradation system, but BQ

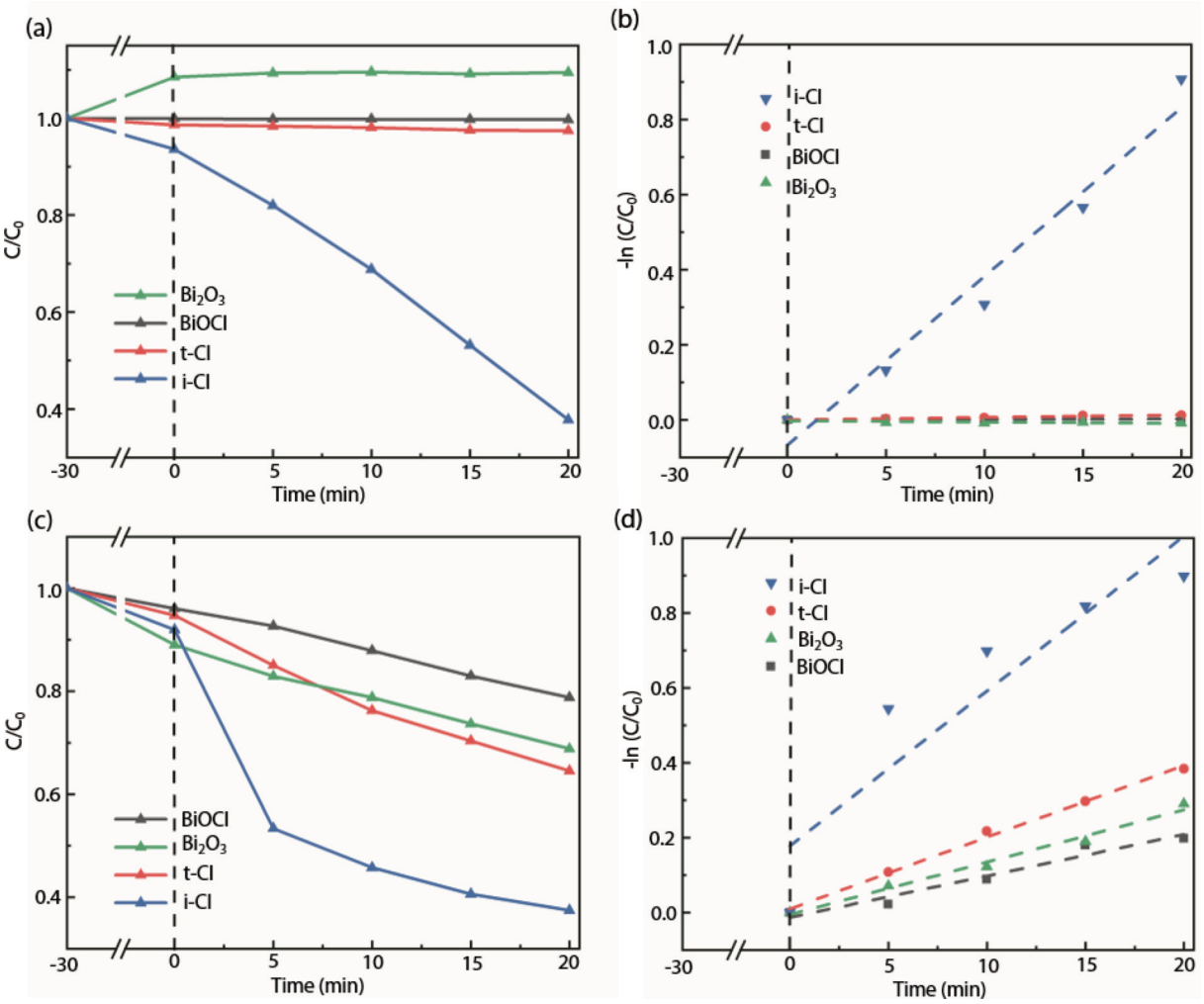

Fig. 6. (Color online) (a) The photocatalytic RhB degradation curves and (b) first-order kinetic fitting of curves of i-Cl, t-Cl, Bi_2O_3, and BiOCl samples in mixed wastewater. (c) The photocatalytic TC degradation curves and (d) first-order kinetic fitting of curves of i-Cl, t-Cl, Bi_2O_3 and BiOCl samples in mixed wastewater.

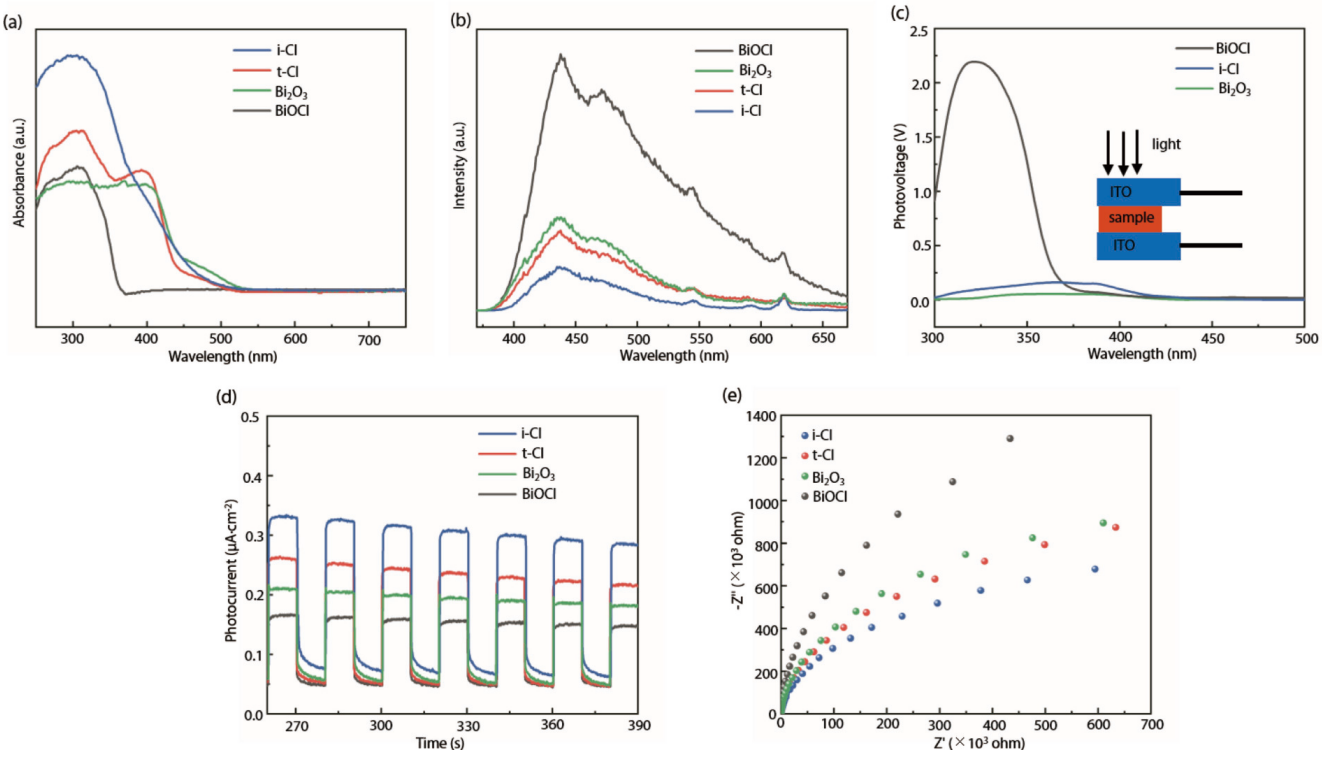

Fig. 7. (Color online) (a) UV-Vis DRS spectra, (b) PL spectra, (c) SPV, (d) photocurrent responses, and (e) the EIS Nyquist plots of the samples.

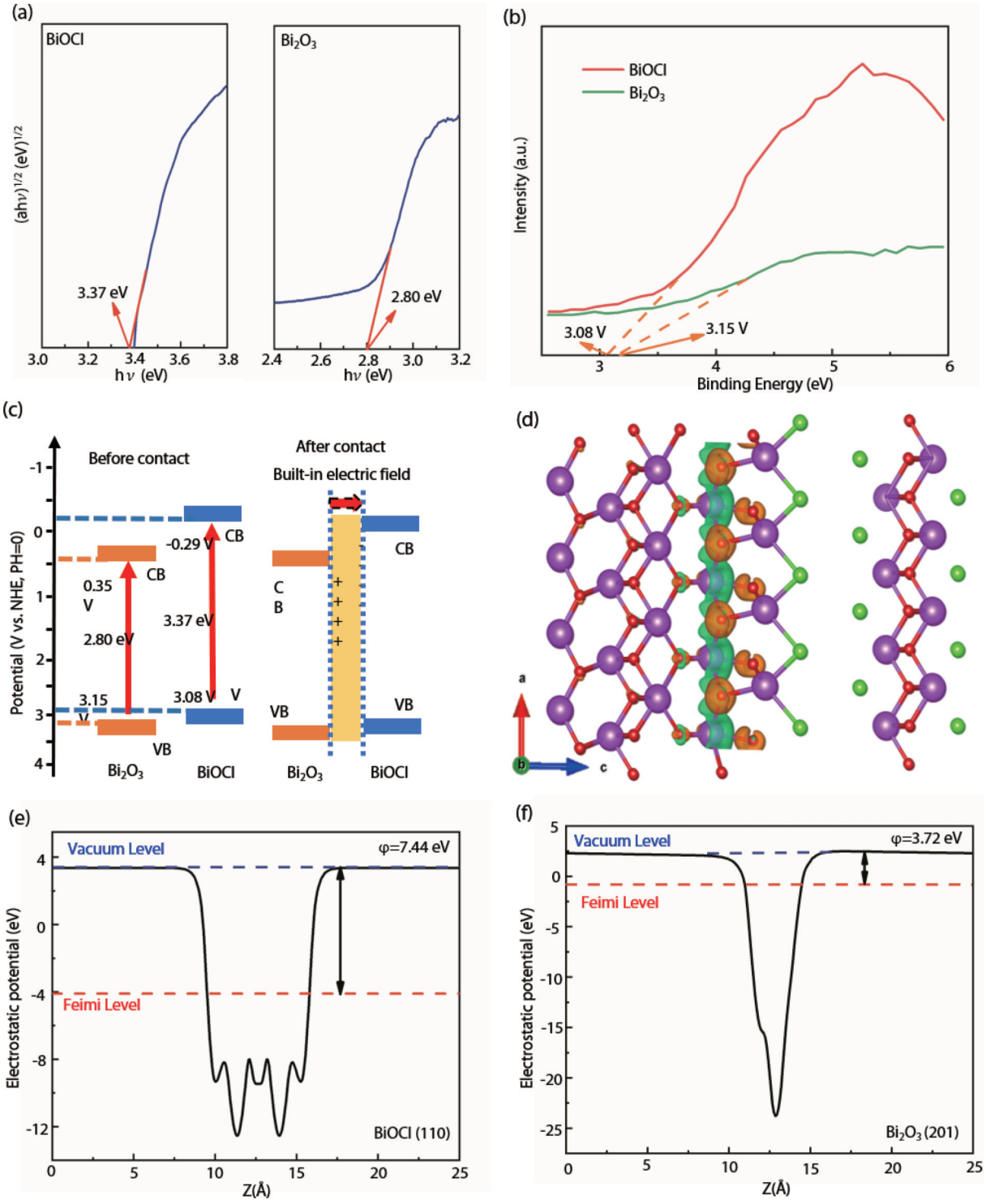

Fig. 8. (Color online) (a) Kubelka-Munk transformed reflectance spectra, (b) VB spectra of BiOCl and Bi_2O_3. (c) Band structures of Bi_2O_3 and BiOCl before and after contact. (d) Charge density difference of BiOCl/Bi_2O_3 heterojunction. The work function of (e) BiOCl (110) and (f) Bi_2O_3 (201).

hardly inhibited the degradation of TC and RhB. The results indicated that h^+ and ·OH are the main active substances in the photocatalytic degradation system. To further confirm the production of the active radical, electron spin resonance (ESR) test was carried out[53]. As shown in Fig. 9(b), no DMPO-·OH signal was detected in this system without visible-light irradiation while the DMPO-·OH signal can be detected under visible light. In addition, the intensity of the DMPO-·OH signal was increased gradually with the irradiation time gone. The results indicated that ·OH was produced after illumination.

Fig. 9(c) shows a plausible mechanism based on the one-photon excitation pathway for the photocatalytic degradation over the i-Cl sample. Under the irradiation of visible light, the photoexcited electrons jumped from the valence band (VB) of Bi_2O_3 to the conduction band (CB) of Bi_2O_3. While the BiOCl fails to be excited by visible light. As the VB position of Bi_2O_3 is more positive than that of BiOCl and the CB position of Bi_2O_3 is more negative than that of BiOCl, the photogenerated holes in the VB of Bi_2O_3 can migrate quickly to the VB of BiOCl and the electrons reserved in the CB of Bi_2O_3, which is beneficial to the effective spatial separation of photogenerated carriers. Our experimental photocatalytic perform-

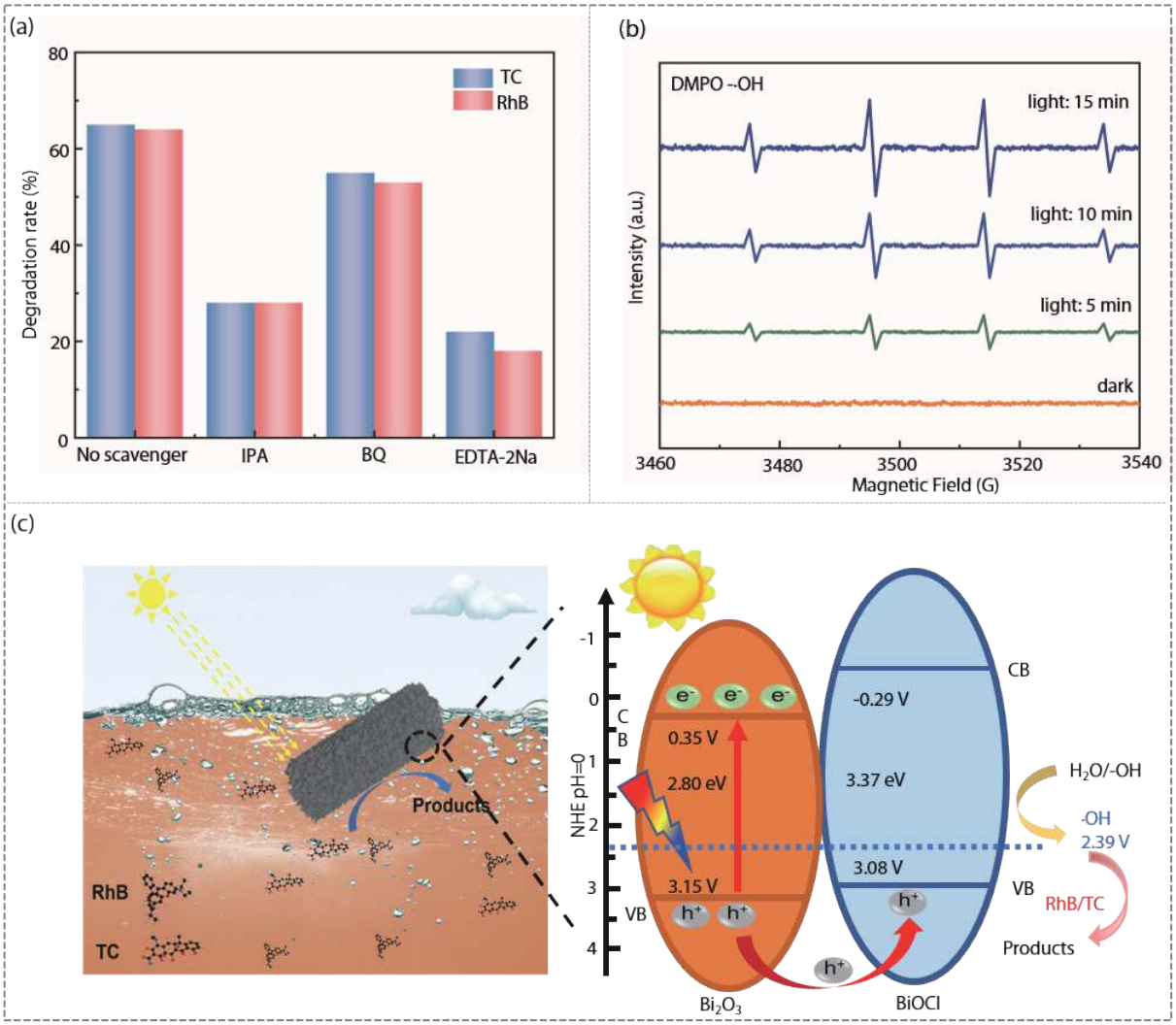

Fig. 9. (Color online) (a) The reactive species trapping experiment and (b) ESR spectra of the i-Cl sample under light irradiation. (c) A plausible mechanism for the photocatalytic degradation of RhB and TC under visible light over the i-Cl sample.

ance for degrading RhB and TC demonstrates that this one-photon excitation on Bi_2O_3 coupled with BiOCl with a large bandgap can make full use of photons, and it is expected to achieve higher theoretical photon utilization efficiency.

Then, the holes in the CB of BiOCl easily react with H_2O to produce hydroxyl radicals (·OH) that serve as reactive oxygen species for the degradation of organic pollutants. The possible degradation steps are as follows:

$$\text{i-Cl} + h\upsilon \rightarrow e^- + h^+, \quad (3)$$

$$H_2O + h^+ \rightarrow H_2O^+ \rightarrow h^+ + OH^-, \quad (4)$$

$$OH^- + h^+ \rightarrow \cdot OH, \quad (5)$$

$$\text{TC/RhB} + \cdot OH \rightarrow \text{Products}. \quad (6)$$

4. Conclusions

In conclusion, the 2D in-plane heterogeneous i-Cl composite composed of BiOCl and Bi_2O_3 was synthesized through one-step calcination of halogen-doped CAU-17 for photocatalytic degradation of RhB and TC by a one-photon excitation pathway. In the design of this in-plane heterojunction, the chemical bond at the interface will induce a strong intrinsic electric field, which will promote the charge separation and transmission of photogenerated carriers. In addition, the matched band structures and the strong intrinsic electric field between BiOCl and Bi_2O_3 accelerate the charge transfer from Bi_2O_3 to BiOCl, constructing a one-photon excitation pathway in nanocomposite photocatalysts for efficiently degrading dyes and antibiotics. The i-Cl sample exhibited enhanced photocatalytic performance of degrading TC and RhB aqueous solutions and mixed wastewater containing TC and RhB compared with pure BiOCl, Bi_2O_3, and a traditional t-Cl composite composed of BiOCl and Bi_2O_3. The degradation rate of the RhB solution reached 90% in 20 min and that of the TC solution reached 70% in 20 min. And in the photocatalytic degradation system for mixed wastewater with TC and RhB, the i-Cl sample also has an excellent RhB and TC removal efficiency of up to 64% and 65% at the same time within 20 min. This work provides a logical strategy to construct other 2D in-plane heterojunctions with a one-photon excitation pathway with enhanced photocatalytic performance.

Acknowledgments

This work was supported by the National Natural Sci-

ence Foundation of China (11874314, 12174157, and 12074150), the Natural Science Foundation of Jiangsu Province (BK20201424), the Modern Agricultural Equipment and Technology Collaborative Innovation Project (XTCX2025), and the Graduate Research and Innovation Projects of Jiangsu Province (KYCX22_3602).

Appendix A. Supplementary materials

Supplementary materials to this article can be found online at https://doi.org/10.1088/1674-4926/44/052701.

References

[1] Zampieri M. The genetic underground of antibiotic resistance. Science, 2021, 371, 783

[2] Gong P, Xu H, Wang C F, et al. Persistent organic pollutant cycling in forests. Nat Rev Earth Env, 2021, 2, 182

[3] Li Q, Pellegrino J, Lee D J, et al. Synthetic group A streptogramin antibiotics that overcome Vat resistance. Nature, 2020, 586, 145

[4] Larsson D G J, Flach C F. Antibiotic resistance in the environment. Nat Rev Microbiol, 2022, 20, 257

[5] Deepracha S, Ayral A, Ogawa M. Acceleration of the photocatalytic degradation of organics by in-situ removal of the products of degradation. Appl Catal B, 2021, 284, 119705

[6] Praxedes F R, Nobre M A L, Poon P S, et al. Nanostructured $K_xNa_{1-x}NbO_3$ hollow spheres as potential materials for the photocatalytic treatment of polluted water. Appl Catal B, 2021, 298, 120502

[7] Keshavarzi N, Antonietti S CM. A new conducting polymer with exceptional visible-light photocatalytic activity derived from barbituric acid polycondensation. Adv Mater, 2020, 32, e1907702

[8] Lin H, Wang J H, Zhao J W, et al. Molecular dipole-induced photoredox catalysis for hydrogen evolution over self-assembled naphthalimide nanoribbons. Angew Chem Int Edit, 2022, 134, e202117645

[9] Wang Y T, Zhu C Z, Zuo G C, et al. 0D/2D Co_3O_4/TiO_2 Z-Scheme heterojunction for boosted photocatalytic degradation and mechanism investigation. Appl Catal B, 2020, 278, 119298

[10] Zhang Q C, Jiang L, Wang J, et al. Photocatalytic degradation of tetracycline antibiotics using three-dimensional network structure perylene diimide supramolecular organic photocatalyst under visible-light irradiation. Appl Catal B, 2020, 277, 119122

[11] Ma M, Wang Z J, Lei Y, et al. An in-depth understanding of photophysics in organic photocatalysts. J Semicond, 2023, 44, 030401

[12] Su H W, Yu X H, Wang W K, et al. A 2D bimetallic Ni-Co hydroxide monolayer cocatalyst for boosting photocatalytic H_2 evolution. Chem Commun, 2022, 58, 6180

[13] Zhao C, Wang Z J, Shu D J, et al. A close step towards industrialized application of solar water splitting. J Semicond, 2020, 41(9), 090401

[14] Wang Y, Wang H, Li J, et al. Facile synthesis of metal-free perylene imide-carbon nitride membranes for efficient photocatalytic degradation of organic pollutants in the presence of peroxymonosulfate. Appl Catal B, 2020, 278, 118981

[15] Shi L, Yin J N, Liu Y R, et al. Embedding Cu_3P quantum dots onto BiOCl nanosheets as a 0D/2D S-scheme heterojunction for photocatalytic antibiotic degradation. Chemosphere, 2022, 309, 136607

[16] Vinoth S, Ong W J, Pandikumar A. Defect engineering of BiOX (X = Cl, Br, I) based photocatalysts for energy and environmental applications: Current progress and future perspectives. Coordin Chem Rev, 2022, 464, 214541

[17] Wu Y Y, Hu Y X, Han M Q, et al. Mechanism insights into the facet-dependent photocatalytic degradation of perfluorooctanoic acid on BiOCl nanosheets. Chem Eng J, 2021, 425, 130672

[18] Zhou P F, Shen Y B, Zhao S K, et al. Synthesis of clinoptilolite-supported $BiOCl/TiO_2$ heterojunction nanocomposites with highly-enhanced photocatalytic activity for the complete degradation of xanthates under visible light. Chem Eng J, 2021, 407, 126697

[19] Wang L L, Yang T, Peng L J, et al. Dual transfer channels of photocarriers in 2D/2D/2D sandwich-like $ZnIn_2S_4$/g-C_3N_4/Ti_3C_2 MXene S-scheme/Schottky heterojunction for boosting photocatalytic H_2 evolution. Chinese J Catal, 2022, 43, 2720

[20] Cao D W, Li M, Zhu J F, et al. Enhancement of photoelectrochemical performance in ferroelectric films via the introduction of an Au buffer layer. J Semicond, 2021, 42, 112701

[21] Wang L L, Tang G G, Liu S, et al. Interfacial active-site-rich 0D Co_3O_4/1D TiO_2 p-n heterojunction for enhanced photocatalytic hydrogen evolution. Chem Eng J, 2022, 428, 131338

[22] Shen T, Shi X K, Guo J X, et al. Photocatalytic removal of NO by light-driven Mn_3O_4/BiOCl heterojunction photocatalyst: Optimization and mechanism. Chem Eng J, 2021, 408, 128014

[23] Mao L B, Liu H, Yao L L, et al. Construction of a dual-functional CuO/BiOCl heterojunction for high-efficiently photoelectrochemical biosensing and photoelectrocatalytic degradation of aflatoxin B1. Chem Eng J, 2022, 429, 132297

[24] Mei J, Tao Y, Gao C, et al. Photo-induced dye-sensitized $BiPO_4$/BiOCl system for stably treating persistent organic pollutants. Appl Catal B, 2021, 285, 119841

[25] Deng P K, Xu Y Y, Xu J, et al. Rationally Designed ZnCd-MOF/Ag_3PO_4 heterojunction for boosted photocatalytic oxygen evolution and in-situ grown of Ag nanoparticles. Res Chem Intermediat, 2022, 48, 2821

[26] Xu Y Y, Xu J, Yan W, et al. Synergistic effect of a noble metal free MoS_2 co-catalyst and a ternary Bi_2S_3/MoS_2/P25 heterojunction for enhanced photocatalytic H_2 production. Ceram Int, 2021, 47, 8895

[27] Zhang H, Tang G G, Wan X, et al. High-efficiency all-solid-state Z-scheme Ag_3PO_4/g-C_3N_4/$MoSe_2$ photocatalyst with boosted visible-light photocatalytic performance for antibiotic elimination. Appl Surf Sci, 2020, 530, 147234

[28] Lin Y, Su W Y, Wang X X, et al. LaOCl-Coupled polymeric carbon nitride for overall water splitting through a one-photon excitation pathway. Angew Chem Int Edit, 2020, 59, 20919

[29] Li B, Peng W, Zhang J, et al. High-throughput one-photon excitation pathway in 0D/3D heterojunctions for visible-light driven hydrogen evolution. Adv Funct Mater, 2021, 31, 2100816

[30] Wang L, Zhao X, Lv D D, et al. Promoted photocharge separation in 2D lateral epitaxial heterostructure for visible-light-driven CO_2 photoreduction. Adv Mater, 2020, 32, e2004311

[31] Fang R Q, Dhakshinamoorthy A, Li Y, et al. Metal organic frameworks for biomass conversion. Chem Soc Rev, 2020, 49, 3638-3687

[32] Han D L, Liu X M, Wu S L, et al. Metal organic framework-based antibacterial agents and their underlying mechanisms. Chem Soc Rev, 2022, 51, 7138

[33] Xu J, He S, Zhang H L, et al. Layered metal–organic framework/graphene nanoarchitectures for organic photosynthesis under visible light. J Mater Chem A, 2015, 3, 24261

[34] Sharma S, Sahu B K, Cao L, et al. Porous nanomaterials: Main vein of agricultural nanotechnology. Prog Mater Sci, 2021, 121, 100812

[35] Zhu S R, Wu M K, Zhao W N, et al. In situ growth of MOF on BiOBr 2D material with excellent photocatalytic activity for dye degradation. Cryst Growth Des, 2017, 17, 2309

[36] Yang L, Xin Y M, Yao C F, et al. In situ preparation of Bi_2WO_6/CAU-17 photocatalyst with excellent photocatalytic activity for dye degradation. J Mater Sci:Mater Electron, 2021, 32, 13382

[37] Wang Q X, Li G. Bi(iii) MOFs: syntheses, structures and applications. Inorg Chem Front, 2021, 8, 572

[38] Li S J, Cai M J, Wang C C, et al. Rationally designed Ta_3N_5/BiOCl S-scheme heterojunction with oxygen vacancies for elimination of tetracycline antibiotic and Cr(VI): Performance, toxicity evaluation and mechanism insight. J Mater Sci Technol, 2022, 123, 177

[39] Bai J W, Li Y, Wei P K, et al. Enhancement of photocatalytic activity of Bi_2O_3–BiOI composite nanosheets through vacancy engineering. Small, 2019, 15, 1900020

[40] Lv X, Yan D Y S, Lam F L, et al. Solvothermal synthesis of copper-doped BiOBr microflowers with enhanced adsorption and visible-light driven photocatalytic degradation of norfloxacin. Chem Eng J, 2020, 401, 126012

[41] Yu C C, Chang H, Sun A C, et al. Stabilization of the β-phase Bi_2O_3 (201) thin film by an ultrathin Bi (001) seeding layer. Vacuum, 2019, 169, 108918

[42] Zhou Q, Huang W, Xu C, et al. Novel hierarchical carbon quantum dots-decorated BiOCl nanosheet/carbonized eggshell membrane composites for improved removal of organic contaminants from water via synergistic adsorption and photocatalysis. Chem Eng J, 2021, 420, 129582

[43] Yang X Y, Zhang Y M, Wang Y L, et al. Hollow β-Bi_2O_3@CeO_2 heterostructure microsphere with controllable crystal phase for efficient photocatalysis. Chem Eng J, 2020, 387, 124100

[44] Xu K Q, Shen J, Zhang S Y, et al. Efficient interfacial charge transfer of BiOCl-In_2O_3 step-scheme heterojunction for boosted photocatalytic degradation of ciprofloxacin. J Mater Sci Technol, 2022, 121, 236

[45] Liu M C, Ye P, Wang M, et al. 2D/2D Bi-MOF-derived BiOCl/MoS_2 nanosheets S-scheme heterojunction for effective photocatalytic degradation. J Environ Chem Eng, 2022, 10, 108436

[46] Ming J T, Liu A, Zhao J W, et al. Hot π-electron tunneling of metal–insulator–COF nanostructures for efficient hydrogen production. Angew Chem Int Edit, 2019, 58, 18290

[47] Yan W, Xu Y Y, Hao S W, et al. Promoting charge separation in hollow-structured C/MoS_2@$ZnIn_2S_4$/Co_3O_4 photocatalysts via double heterojunctions for enhanced photocatalytic hydrogen evolution. Inorg Chem, 2022, 61, 4725

[48] Huang T, Lin X, Liu Y, et al. Molecular engineering of fully conjugated sp^2 carbon-linked polymers for high-efficiency photocatalytic hydrogen evolution. Chemsuschem, 2020, 13, 672

[49] Li S J, Wang C C, Liu Y P, et al. Photocatalytic degradation of antibiotics using a novel Ag/Ag_2S/Bi_2MoO_6 plasmonic p-n heterojunction photocatalyst: Mineralization activity, degradation pathways and boosted charge separation mechanism. Chem Eng J, 2021, 415, 128991

[50] Lee J H, Lee Y, Bathula C, et al. A zero-dimensional/two-dimensional Ag-Ag_2S-CdS plasmonic nanohybrid for rapid photodegradation of organic pollutant by solar light. Chemosphere, 2022, 296, 133973

[51] Park S H, Kim T, Kadam A N, et al. Synergistic photocatalysis of Z-scheme type Fe_2O_3/g-C_3N_4 heterojunction coupled with reduced graphene oxide. Sur Inter, 2022, 30, 101910

[52] Yao L, He X M, Lv J, et al. Efficient degradation of ciprofloxacin by Co_3O_4/Si nanoarrays heterojunction activated peroxymonosulfate under simulated sunlight: Performance and mechanism. J Environ Chem Eng, 2022, 10, 107397

[53] Tang G G, Chen W T, Wan X, et al. Construction of magnetic Fe_3O_4 nanoparticles coupled with flower-like $MoSe_2$ nanosheets for efficient adsorptive removal of methylene blue. Colloid Surface A, 2019, 587, 124291

Mengchi Liu is a postgraduate student in the school of physics and electronic engineering, jiangsu university, majoring in physics. At present, the research direction is photocatalysis, and the specific content of the research is in-situ growth of Bi-based semiconductor heterojunction with Bi-MOF as a precursor, thereby improving the performance of photocatalysis sewage treatment.

Yuanping Chen received the Ph.D degree from Xiangtan University in 2007. He is currently a professor, doctoral supervisor, and a "double-creative talent" in Jiangsu Province, serving as Executive Vice Dean of School of Physics and Electronic Engineering. He is mainly engaged in the research of material properties, principles and applications, especially in the fields of topological materials, quantum transport, optoelectronic properties, etc. He has achieved a series of innovative results and published more than 100 high-level papers in *Nat Energy*, *Nat Commun*.